ACS APPLIED MATERIALS & INTERFACES

Research Article

www.acsami.org

Highly Efficient One-Dimensional ZnO Nanowire-Based Dye-Sensitized Solar Cell Using a Metal-Free, D−π−A-Type, Carbazole Derivative with More than 5% Power Conversion

Dipankar Barpuzary,[†] Anindya S. Patra,[†] Jayraj V. Vaghasiya,[‡] Bharat G. Solanki,[‡] Saurabh S. Soni,*[,‡] and Mohammad Qureshi*[,†]

[†]Materials Science Laboratory, Department of Chemistry, Indian Institute of Technology Guwahati, Guwahati-781039, Assam, India

[‡]Department of Chemistry, Sardar Patel University, Vallabh Vidyanagar-388120, Gujarat, India

Supporting Information

ABSTRACT: Hydrothermally grown one-dimensional ZnO nanowire (1D ZnO NW) and a newly synthesized metal-free, D−π−A type, carbazole dye (SK1) sensitizer-based photovoltaic device with a power conversion efficiency (PCE) of more than 5% have been demonstrated by employing the cobalt tris(2,2′-bipyridyl) redox shuttle. A short-circuit current density (J_{sc}) of ∼12.0 mA/cm^2, an open-circuit voltage (V_{oc}) of ∼719 mV, and a fill factor (FF) of ∼65% have been afforded by the 1D ZnO NW-based dye-sensitized solar cell (DSSC) incorporating $[Co(bpy)_3]^{3+/2+}$ complex as the one-electron redox mediator. In contrast, the identical DSSC with traditional I_3^-/I^- electrolyte has shown a J_{sc} ≈ 12.2 mA/cm^2, a V_{oc} ≈ 629 mV, and a FF ≈ 62%, yielding a PCE of ∼4.7%. The persuasive role of the inherent superior electron transport property of 1D ZnO NWs in enhancing the device efficiency is evidenced from the impoverished performance of the DSSCs with photoanodes fabricated using ZnO nanoparticles (NPs). The DSSCs having ZnO NP-based photoanodes have achieved the PCEs of ∼3.6% and ∼3.2% using cobalt- and iodine-based redox electrolytes, respectively. The electronic interactions between the SK1 sensitizer and ZnO (NWs and NPs) to induce the photogenerated charge transfer from SK1 to the conduction band (CB) of ZnO are evidenced from the significant quenching of photoluminescence and exciton lifetime decay of SK1, when it is anchored onto the ZnO architectures. The energetics of the SK1 dye molecule are estimated by combining the spectroscopic and electrochemical techniques. The electronic distributions of SK1 dye molecule in its HOMO and LUMO energy levels are interpreted using density functional theory (DFT)-based calculations. The electron donor−π linker−acceptor (D−π−A) configuration of SK1 dye provides an intramolecular charge transfer within the molecule, prompting the electron migration from the carbazole donor to cyanoacrylic acceptor moiety via the oligo-phenylenevinylene linker group. The D−π−A-mediated electron movement witnesses the favorable photoexcited electron transfer from the LUMO of SK1 dye to the CB of ZnO through the carboxyl anchoring group.

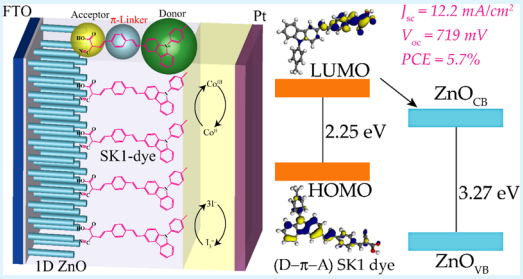

KEYWORDS: *dye-sensitized solar cell, one-dimensional ZnO nanowires, ZnO nanoparticles, D−π−A carbazole dye, frontier molecular orbital, DFT calculations*

1. INTRODUCTION

Dye-sensitized solar cells (DSSCs) have emerged as an efficient and promising candidate for the solar to electrical energy conversion devices. The outstanding performance efficacy of these cells primarily depends on the development or modification of the key components: (i) semiconductor nanomaterials having inherently efficient electron transport properties, (ii) broad solar light absorbing molecules or dyes that harvest the sunlight to excite electrons and inject them into the semiconductors, and (iii) noncorrosive redox mediators with enhanced dye regeneration and open-circuit voltage.[1,2] Although the power conversion efficiency (PCE) of DSSCs employing the porphyrin dye and cobalt(III/II)-based redox mediators has reached a maximum of 13% within the past two decades since the pioneering work proposed by O'Regan and Grätzel in 1991, improvements are still needed for their commercialization.[3−5] The fabrication of cost-effective photovoltaic devices on a large scale has been the prime focus among the researchers by exploring innovative ideas depending on the availability of existing or newly developed materials. So far, the maximum enhancement in the efficiency of the DSSCs has been achieved by using the metal-based dyes such as N3, N719, porphyrins, phthalocyanines, etc.; however, most of them are expensive and laborious to synthesize with tricky purification routes.[6] In this respect, an alternate way to improve the DSSC performance is to use the metal-free organic dyes or their donor−acceptor (D−A) combinations as the sensitizers in conjugation with the cobalt(III/II)-based electrolytes.[7,8] Several

Received: April 29, 2014
Accepted: July 16, 2014
Published: July 16, 2014

Scheme 1. Synthesis Procedure of 2-Cyano-3-(4-(2-(9-*p*-tolyl-9*H*-fluoren-6-yl)vinyl)phenyl) Acrylic Acid Dye and the Predicted Donor−π Linker−Acceptor (D−π−A) Groups[a]

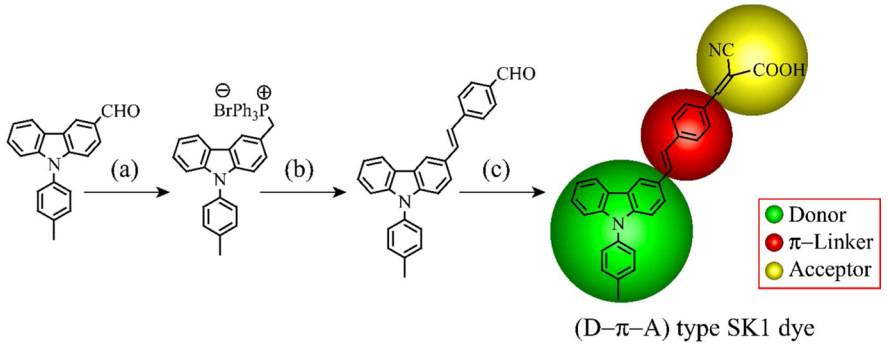

[a]Reagents and conditions: (a) 0.4 equiv of $NaBH_4$ in THF followed by triphenylphosphine hydrobromide in dichloromethane, (b) terephthaldehyde, sodium ethoxide in ethanol at 5 °C, and (c) cyanoacetic acid and catalytic amount of piperidine in acetonitrile.

metal-free derivatives of indoline, carbazole, thiafulvene, coumarin, etc., have shown promising PCEs approaching 10% in DSSCs due to their low band gap, high molar extinction coefficients, and facile molecular design.[9−12] An advantage among the organic dyes is that they can be easily tuned by incorporating light absorbing groups of different type into the organic framework, thereby enhancing the overall molar extinction coefficient. In addition, facile molecular engineering of the organic dye sensitizers by employing π-conjugated linker groups between the electron donor and acceptor units improves the proficiency of donor−π linker−acceptor (D−π−A)-based DSSCs.[13,14] Moreover, it is noteworthy that the use of cobalt complexes as the redox electrolytes in DSSCs rivals the traditional iodide/triiodide (I_3^-/I^-) system due to their lower visible light absorption, noncorrosive nature, and higher redox potential, as compared to that of I_3^-/I^-, which are paramount to enhance the device efficiencies.[15−19] Chao et al. have reported TiO_2-based devices using a series of carbazole-based dyes incorporating the D−π−A concept to achieve a PCE up to ∼5.2% along with a very high open-circuit voltage (V_{oc}) beyond 1000 mV by employing bromine/bromide (Br^-/Br_3^-) and I_3^-/I^--based redox mediators.[20−22] Simultaneously with the development of organic dyes and electrolytes, semiconductor materials have also been thoroughly investigated for their potential role in DSSCs. In the recent past, ZnO has reaped extensive applications as the electron transport layer over the much studied TiO_2 due to its higher electron mobility, faster electron transport, and ease of synthesis in various dimensions and morphologies.[23−25] In particular, one-dimensional (1D) nanowires (NWs) have shown intense interest in the fabrication of photovoltaic devices due to their unique geometry providing direct and effective pathways for charge transport, lower electron hopping, and higher interfacial area.[26−29] For the practical applications, high band gap limitation of ZnO, to absorb the visible light, can be readily overcome by sensitizing with a suitable dye or semiconductor, which can transfer their photoexcited electrons to the conduction band (CB) of ZnO.[30,31] For a better device performance, dye-sensitization process should be carried out with great precision with respect to the dipping time and dye concentration in case of ZnO-based DSSCs when the dye contains acidic (−COOH) linker groups. Considering all of these key points, herein, we report a highly efficient photovoltaic device involving hydrothermally grown 1D ZnO NWs[32] sensitized by a metal-free carbazole dye (SK1), 2-cyano-3-(4-(2-(9-*p*-tolyl-9*H*-fluoren-6-yl)vinyl)phenyl)acrylic acid.

We have synthesized (using Wittig reaction) the organic dye, SK1, containing a carbazole unit (donor) and a cyanoacrylic acid unit (acceptor) linked via a π-conjugated oligo-phenylenevinylene group as shown in Scheme 1. The as-synthesized D−π−A-type dye (SK1) provides intramolecular charge transfer from the donor to acceptor site within the molecule at the lowest-unoccupied molecular orbital (LUMO) level. In addition, the carboxyl group of the acceptor moiety acts as the anchoring group for the attachment of dye to ZnO architectures. The photoexcited electron transfer from the excited state of SK1 to the CB of ZnO in the fabricated photoanodes of DSSCs is monitored using steady-state photoluminescence (PL) and time-resolved PL decay measurements. The outweighed device performance efficiencies of the DSSCs based on 1D ZnO NWs in contrast to ZnO nanoparticles (NPs) are investigated by employing cobalt(III/II) as well as I_3^-/I^- redox shuttles.

2. EXPERIMENTAL SECTION

2.1. Materials. Zinc acetate dihydrate (Merck), ethanolamine (Himedia), 2-methoxyethanol (Himedia), PTFE syringe filter (Axiva Sichem Biotech, India), zinc nitrate hexahydrate (Merck), hexamethylenetetramine (Himedia), zinc chloride (Merck), sodium hydroxide (Merck), terpineol (Himedia), poly(ethylene glycol)-blockpoly-(propylene glycol)-*block*-poly(ethylene glycol) or PEG−PPG−PEG triblock copolymer (Aldrich), hexachloroplatinic acid (H_2PtCl_6, Aldrich), lithium iodide (Aldrich), iodine (Merck), guanidium thiocyanate (Aldrich), cobalt chloride hexahydrate (Merck), 2,2′-bipyridyl (bpy, Aldrich), bromine (Merck), potassium hexafluorophosphate (Aldrich), 4-*tert*-butylpyridine (Himedia), acetonitrile (HPLC grade, Merck), valeronitrile (Aldrich), sodium borohydride (Merck), tetrahydrofuran (Merck), dichloromethane (Merck), sodium sulfate (Merck), triphenylphosphinehydrobromide (Merck), terpthaldehyde (Merck), ethanol (TMEDA), methanol (Merck), and sodium ethoxide (Merck) were used as received without further purification. FTO-coated glass (surface resistivity ∼7Ω/□, Aldrich, USA), 0.2 μm PTFE filter paper (Axiva, India), and low-temperature thermoplastic sealant were purchased. Milli-Q grade water (18.2 MΩ cm) was used for all of the experiments.

2.1.1. Synthesis of SK1 Dye. Following the protocol mentioned in Scheme 1, the aldehyde was first reduced to the corresponding alcohol by treating with sodium borohydride in tetrahydrofuran at 5 °C, followed by stirring at room temperature for 6 h. The reaction mass was then poured into cold water and extracted in dichloromethane. The organic layer was dried using anhydrous sodium sulfate, and the solvent was removed under vacuum to yield the oil. The Wittig salt

was prepared from this alcohol using triphenylphosphinehydrobromide in dichloromethane. A white colored Wittig salt was separated out upon the addition of diethyl ether. It was condensed with terpthaldehyde in ethanol using sodium ethoxide as a base under cold conditions (5−10 °C). This reaction mass was stirred at room temperature for 2 h and then poured into water and neutralized with dilute hydrochloric acid to get the yellow colored solid crude. The solid was dissolved in tetrahydrofuran in the presence of a catalytic amount of iodine and refluxed for 4 h. The reaction mass was then poured into diluted alkali solution and the solid was separated out, which was purified using column chromatography (EtOAc:*n*-hexane, 3:7, v/v). The purified aldehyde was dissolved in acetonitrile and cyanoacetic acid, and a catalytic amount of piperidine was added. The reaction mass was allowed to reflux for 3 h, and then solvent was removed under vacuum. The dried crude was finally purified using column chromatography (EtOAc:*n*-hexane, 1:1, v/v) to yield an orange solid product. The ^{1}H NMR (in $CDCl_3$) and ^{13}C NMR (in DMSO-d_6) spectra of SK1 dye are shown in Figures S1 and S2 (see the Supporting Information), respectively. ^{1}H NMR ($CDCl_3$, 400 MHz) δ (ppm): 11.00 (s, 1H), 8.30 (s, 2H), 8.20 (s, 2H), 7.86 (s, 1H), 7.72 (s, 3H), 7.42 (d, 4H), 7.41 (d, 2H), 7.40 (d, 2H), 7.20 (d, 2H), 1.90 (s, 3H). ^{13}C NMR (DMSO-d_6, 400 MHz) δ (ppm): 21.09, 64.05, 116.90, 125.24, 126.52, 127.55, 127.66, 128.41, 128.69, 129.47, 130.28, 130.38, 130.87, 131.09, 132.10, 132.19, 134.04, 145.79, 153.23. The mass spectrum of SK1 dye is shown in Figure S3 (see the Supporting Information). MS (ESI) m/z: $[M]^+$ for $C_{31}H_{22}N_2O_2$, calcd, 454.16; found, 453.80. Anal. Calcd for $C_{31}H_{22}N_2O_2$: C, 81.83; H, 5.10; N, 6.16; O, 7.03. Found: C, 81.70; H, 5.13; N, 6.10; O, 7.07.

2.1.2. Deposition of ZnO Seed Layer. For the deposition of ZnO seed layer, FTO substrates having sheet resistance ∼7Ω/□ (Aldrich, U.S.) were first cleaned with soap solution and plenty of distilled water. The substrates were further cleaned under ultrasonic treatment for 15 min in each of acetone and iso-propanol. The substrates were taken out and dried by blowing argon gas and then were subjected to ozone treatment at 60 °C for 30 min in a Novascan UV/ozone probe chamber prior to spin coating the ZnO seed solution. The ZnO seed solution was prepared by dissolving $Zn(CH_3COO)_2{\cdot}2H_2O$ (0.210 g, 300 mM) and ethanolamine (0.055 mL, 300 mM) in 3 mL of 2-methoxyethanol. The solution was stirred for 8 h at room temperature and filtered through a 0.2 μm PTFE syringe filter. The filtered seed solution was spin coated on the ozonized FTO substrates and annealed at 170 °C for 10 min under ambient conditions. The process was repeated once more to get a uniform ZnO seed layer, which acts as the platform for vertically aligned growth of ZnO NWs.

2.1.3. Growth of ZnO Nanowires. The growth of 1D ZnO NWs was performed on the ZnO seed layer coated FTO substrates by a hydrothermal route.[32] First, a solution of $Zn(NO_3){\cdot}6H_2O$ (50 mM) and hexamethylenetetramine (50 mM) in 25 mL of deionized water was taken in the Teflon-lined stainless steel autoclave vessel (30 mL) and stirred to get a clear solution. The ZnO seeded substrates were then immersed (FTO side down) into the solutions separately. The autoclaves were sealed and subjected to heat at 90 °C in an electronic oven for 1.5 h for the growth of ZnO NWs. The autoclaves were cooled to room temperature, and the FTO substrates were taken out, and rinsed thoroughly in ethanol and Milli-Q water. The substrates were then annealed at 175−200 °C for 10 min. These ZnO NW grown FTO substrates were further used for SK1 dye-sensitization. Bare ZnO NWs in the absence of any ZnO seed layer were synthesized hydrothermally following the reported procedure.[33] $Zn(NO_3)_2{\cdot}6H_2O$ (0.446 g) and NaOH (1.20 g) were dissolved in distilled water to make a 3.0 mL solution (Zn^{2+}:OH^- = 1:20). The solution was then mixed with 0.5 mL of distilled water, 30 mL of ethanol, and 5.5 mL of ethylenediamine and sonicated for 30 min. The solution mixture was transferred to a Teflon-lined stainless steel autoclave and heated at 180 °C for 20 h in an electronic oven. The autoclave was allowed to cool to room temperature, and the solid product was washed with distilled water and ethanol several times. Finally, the sample was dried in a vacuum oven at 60 °C for 4 h in the electronic oven.

2.1.4. Synthesis of ZnO Nanoparticles. The synthesis of ZnO nanoparticles (NPs) was carried out by following a previously reported procedure.[34] $ZnCl_2$ (1.1 g, 40 mmol) was dissolved in 40.0 mL of distilled water and heated to 90 °C under gentle magnetic stirring. An aqueous solution of 5 M NaOH (3.2 mL) was then added slowly, and the mixture was stirred at 90 °C for another 30 min. The solution was allowed to cool to room temperature, and the settled precipitates were separated by discarding the supernatant liquid. The solid product was washed with plenty of distilled water to remove NaCl completely (confirmed by $AgNO_3$ test). The purified particles were then dispersed in iso-propanol under an ultrasonic bath for 10 min at room temperature. The product was collected by centrifugation and then calcinated at 250 °C for 5 h in a muffle furnace to get the ZnO NPs.

2.1.5. Synthesis of Cobalt Complexes. The cobalt(II) and cobalt(III) metal complexes with 2,2′-bipyridyl (bpy) ligand were synthesized by following the protocol reported earlier by Liu et al.[35] For the typical synthesis of $[Co(bpy)_3](PF_6)_2$, $CoCl_2{\cdot}6H_2O$ (0.25 g) was dissolved in 5.0 mL of distilled water. A solution of 2,2′-bipyridyl (0.55 g) in methanol was then slowly (dropwise) added to the aqueous solution of cobalt under magnetic stirring. The reaction mixture was allowed to stir for another 10 min. An aqueous solution of KPF_6 (1.2 g) was then added to precipitate the Co(II) complex. The solid product was filtered, washed with water, and dried in a vacuum to isolate the $[Co(bpy)_3](PF_6)_2$ solid.

The complex $[Co\ (bpy)_3](PF_6)_3$ was synthesized via slight modification of the above procedure. $CoCl_2{\cdot}6H_2O$ (0.25 g) was dissolved in 5.0 mL of distilled water, followed by the dropwise addition of methanolic solution of 2,2′-bipyridyl (0.55 g) under magnetic stirring. After 10 min of stirring, an equivalent molar concentration of Br_2 solution in methanol was added slowly, and the reaction mixture was allowed to stir for 10 min. An orange colored precipitate appeared, which was then discarded by filtering the reaction mixture to get a clear solution. The solvent was evaporated by distillation under reduced pressure, and the residue was dissolved in methanol (15.0 mL). Finally, an aqueous solution of KPF_6 (1.2 g) was added under magnetic stirring to precipitate out the Co(III) complex. The product was filtered, washed with water, and dried in a vacuum to yield the $[Co(bpy)_3](PF_6)_3$ solid.

2.1.6. Material Characterization. The powder X-ray diffraction (XRD) patterns were recorded using Bruker D8 Advance X-ray diffractometer with Cu K_α (λ = 1.54 Å) at 40 kV operating voltage and 40 kA operating current. A scan rate of 0.1 deg/s was fixed to analyze the XRD patterns of the samples within the 2θ range of 10−70°. The ultraviolet−visible (UV−vis) diffused reflectance absorption (DRS) spectra were recorded via a JASCO model V-650 spectrophotometer equipped with a 150 nm integrating sphere and $BaSO_4$ as the standard internal reference. The surface morphology of the samples was investigated by scanning electron microscopy (SEM) using the Leo model 1430vp instrument at an operating voltage of 10 kV and field-emission SEM (FESEM) using a Zeiss (Gemini) instrument with an operating voltage of 3−5 kV. The transmission electron microscopy (TEM) analysis was carried out using a JEOL JEM 2100 microscope at 200 kV operating voltage. The Fourier transform infrared spectroscopy (FTIR) measurements were carried out using a PerkinElmer FTIR instrument. The photoluminescence (PL) measurements were carried out using a Horiba−Jobin Yvon Fluoromax 4P spectrophotometer. The time-resolved PL (TRPL) measurements to determine the exciton lifetimes of the samples are recorded in a LifeSpec II Edinburgh instrument with a lamp frequency of 5 MHz. The neodymium-doped yttrium aluminum garnet (Nd:YAG) laser was used to excite the samples at a wavelength of 405 nm. The cyclic voltammetry (CV) measurements were carried out using CH instruments model CHI600E, Inc., Austin, TX. The CV detection of metal-free carbazole dye (SK1) was performed by using a three-electrode system, on a 2 mm platinum disk as the working electrode, platinum wire as the counter electrode, and nonaqueous Ag/Ag^+ reference electrode as the reference electrode. The redox peaks were calibrated using ferrocene/ferrocenium (Fc/Fc^+) system as the standard. The current density−voltage (J_{sc}−V) performance parameters of the fabricated DSSCs were recorded using Keithley Sourcemeter series 2420 under the darkness and at 100 mW/cm^2 artificial solar illumination. The ozone-free xenon short arc lamp (450 W), fitted with a Newport Oriel Sol3A solar

simulator, produced the standard solar spectrum using the AM 1.5G filter. A standard silicon photovoltaic cell was used to calibrate the intensity of the arc lamp. The incident photon-to-current conversion efficiency (IPCE) of the devices was recorded using Newport Oriel IQE-200, where a 250 W quartz tungsten halogen (QTH) lamp was used as the light source. The QTH lamp was coupled to a Cornerstone monochromator to create the scanning monochromatic light. The light was then passed through the optical chopper, and the signal was amplified by Merlin lock-in amplifier unit and finally detected by the detector. The BET surface area analysis was carried out using Quantachrome surface area analyzer instrument model Autosorb-IQ MP. The electrochemical impedance spectroscopy (EIS) measurements were performed using CH instruments model CHI680E, Inc., Austin, TX. ^{1}H NMR and ^{13}C NMR spectra of SK1 dye molecule were recorded using a 400 MHz Bruker Advance NMR instrument. Mass spectrum of SK1 dye molecule was obtained using a mass spectrometer.

2.1.7. Device Fabrication and Characterization. For the 1D ZnO NW-based DSSC fabrication, 1D ZnO NW grown FTO substrates were first immersed into a 0.3 mM SK1 dye solution in anhydrous ethanol:dichloromethane (1:1, v/v) for 8 h for the sensitization. The substrates were taken out from the solvent, rinsed in ethanol, and dried under hot air blow, which then acted as the photoanode. Again, for the ZnO NP-based photoanode fabrication, first, a ZnO paste was obtained by mixing and grinding ZnO NPs (0.5 g), terpineol (2.5 mL), and triblock PEG−PPG−PEG copolymer (1.5 mL) in an agate mortar. The ZnO paste was coated by using doctor blade technique over the precleaned and ZnO seed layered FTO substrates. The substrates were then calcinated at 450 °C for 1 h to obtain the ZnO NP films with thickness ∼8−10 μm, as confirmed by the surface profilometer. These substrates were then dipped in the SK1 dye solution for 8 h, taken out to wash with ethanol, and dried under hot air blow. In the present work, the dipping time for sensitization of ZnO NW and NP films was set at 8 h for a dye concentration of 0.3 mM, which was carried out by following the study on the effect of dye loading on ZnO films as reported by Chou et al.[36] On the basis of their report, we have observed an optimum adsorptivity of SK1 dye over ZnO architectures, as evidenced from the FTIR and chemisorption measurements. However, concerning the carboxylic group present in the dye molecule, the tendency for a slight decomposition of ZnO to occur cannot be ruled out completely. The amount of adsorbed dye was estimated using adsorption−desorption experiments of the 1D ZnO NW and ZnO NP films after dye sensitization by following the reported procedure.[37] Each of the sensitized films was immersed in a 0.1 mM NaOH solution in a 1:1 ethanol:water mixture, and then the solution was collected and the UV−vis absorbance measured. The concentration of the desorbed dye per cm^2 film area was then calculated from its molar extinction coefficient using Beer's law. For the counter electrode preparation, a 50 mM H_2PtCl_6 solution in ethanol was spin coated on precleaned, ozonized FTO substrates, followed by the calcination at 450 °C for 10 min. The photovoltaic devices were constructed by sandwiching the photoanode and counter electrodes using low-temperature thermoplastic sealant (thickness ∼50 μm). The electrolyte solution was then inserted after sealing the two electrodes to complete the device. The fabricated devices were stored under the dark conditions for 24 h prior to carry out the J_{sc}−V and IPCE measurements. It should be mentioned that an active area of ∼0.16 cm^2 was fixed for all of the devices, for which the deposition of 1D ZnO NW (hydrothermal growth) and ZnO NP (doctor blade technique) films on FTO substrates prior to dye sensitization was carried out in an area of 0.16 cm^2 using a mask. The Co(III/II) electrolyte solution was prepared by dissolving 0.2 M $[Co(bpy)_3](PF_6)_2$, 0.02 M $[Co(bpy)_3](PF_6)_3$, and 0.5 M 4-*tert*-butylpyridine in an acetonitrile:valeronitrile (9:1, v/v) solvent mixture. Similarly, the I_3^-/I^- electrolyte solution was prepared by dissolving 0.5 M LiI, 0.05 M I_2, 0.1 M guanidium thiocyanate, and 0.5 M 4-*tert*-butylpyridine in an acetonitrile:valeronitrile (9:1, v/v) solvent mixture.

3. RESULTS AND DISCUSSION

3.1. Powder X-ray Diffraction Analysis. The phase purity of the as-synthesized ZnO NWs and NPs was investigated by using powder X-ray diffraction (XRD) measurements. It can be seen from Figure 1a that the powder XRD pattern of 1D ZnO

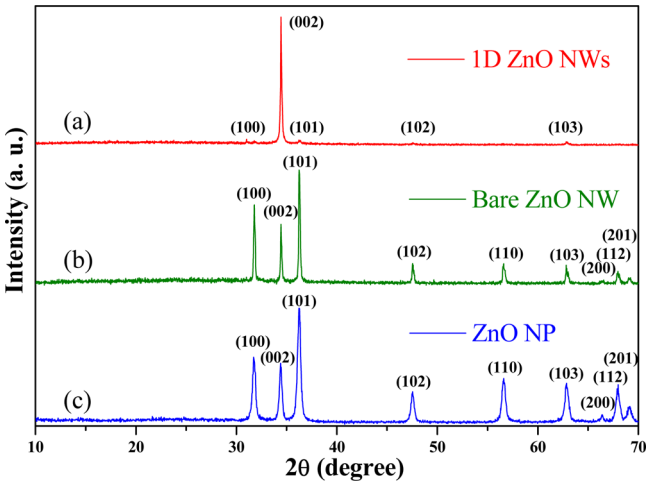

Figure 1. Powder X-ray diffraction patterns for (a) templated growth of one-dimensional ZnO on ZnO seeded glass substrate (please note the preferential growth along the (002) lattice plane), (b) hydrothermally grown bare ZnO nanowires, and (c) ZnO nanoparticles.

NWs (red line) grown over ZnO seed layer shows a strong appearance of (002) diffraction peak at a 2θ of 34.6°. This confirms the characteristic 1D growth of ZnO NWs along the *c*-axis normal to the FTO substrate. The XRD pattern shows that all of the observed diffraction peaks including the lattice plane (100), (002), (101), (103), and (104) are indexed to the formation of hexagonal phase of ZnO ($P6_3mc$ space group symmetry) with the calculated lattice constants of a = 0.3144 nm and c = 0.5108 nm (JCPDS file card no. 36-1451).[38,39] The preferential orientation of 1D ZnO NWs grown over the ZnO seed layered substrates is further confirmed by comparing the XRD pattern with that of hydrothermally synthesized bare 1D ZnO NWs (green line). From trace (b) in Figure 1, the observed lattice planes (100), (002), (101), (102), (110), (103), (200), (112), and (201) for the bare ZnO NWs can be indexed to the formation of hexagonal wurtzite crystalline phase with $P6_3mc$ space group symmetry and lattice constants of a = 0.3247 nm and c = 0.5201 nm (JCPDS file card no. 05-0664). It is clearly observed that the characteristic highest intensity diffraction peak originating from the (002) lattice plane of 1D ZnO NW is absent in the powder XRD pattern recorded for bare 1D ZnO NWs. Trace (c) in Figure 1 shows the crystal planes (100), (002), (101), (102), (110), (103), (200), (112), and (201) for ZnO NPs (blue line), which are indexed to the formation of its hexagonal phase with the calculated lattice constants of a = 0.3249 nm and c = 0.5205 nm. The average crystallite sizes of 1D ZnO NWs and ZnO NPs are estimated using the Debye−Scherrer formula $D = (0.9 \times \lambda)/(\beta \times \cos\theta)$, where λ, θ, and β are the X-ray wavelength (0.154 nm), Bragg diffraction angle, and full width at half-maximum (fwhm), respectively. Considering the maximum intensity planes, (002) for 1D ZnO NW and (101) for ZnO NPs, from the respective XRD patterns, the average crystallite sizes are found to be ∼48.9 nm (1D ZnO NW) and ∼51.8 nm (ZnO NP).

3.2. UV–Vis Diffuse Reflectance Absorption Spectra.

Figure 2 illustrates the normalized UV–vis diffuse reflectance spectra (DRS) of SK1 dye thin-film spin-coated on FTO (SK1), SK1-sensitized ZnO NPs film on FTO (SK1-ZnO NP), and SK1-sensitized 1D ZnO NWs film on FTO (SK1-1D ZnO NW). All of the spectra are recorded as a function of wavelength in the scan range of 300–800 nm against blank FTO substrate as a reference. The absorption spectrum of SK1 dye thin-film (black line) shows its maximum absorbance in the range of 350–550 nm with a high molar extinction coefficient (ε) of 3.42 × 10^4 M^{-1} cm^{-1}. The characteristic absorption spectrum of ZnO NPs (blue line) shows a steep absorption edge at ∼384 nm. Similarly, an absorption steep at ∼378 nm (red line) is observed for 1D ZnO NWs. Notably, there is a slight red shift that occurs in the DRS spectrum of ZnO NPs in contrast to 1D ZnO NWs, which is ascribed to the lower size dimension of ZnO NPs as compared to that of the NWs. In addition, this red shift is further confirmed by the estimated band gaps of ZnO NPs and 1D NWs as interpreted from the UV–vis data using the Tauc plot, where $(\alpha h\nu)^2$ is plotted against the photon energy ($h\nu$).[34] The band gaps of ZnO are calculated using Tauc's relationship for optical band gap following eqs 1 and 2.

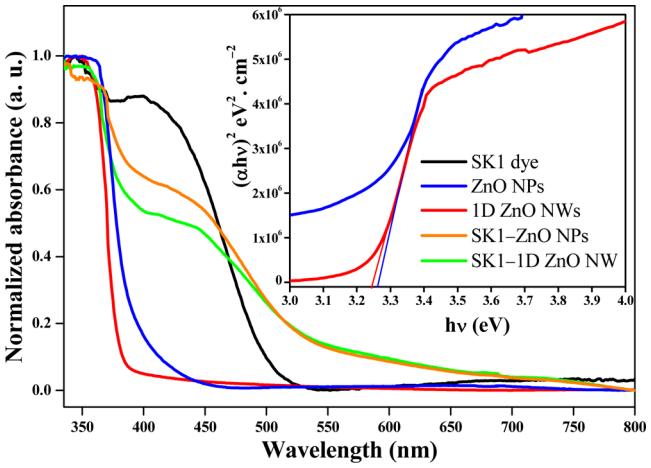

Figure 2. Normalized UV–vis diffused reflectance spectra of SK1 dye (black line), ZnO nanoparticles (blue line), 1D ZnO nanowires (red line), SK1-sensitized ZnO NPs (orange line), and SK1-sensitized 1D ZnO NWs (green line) on FTO. Inset shows the Tauc plots to estimate the band gap of ZnO nanoparticle film (blue line) and 1D ZnO nanowires (blue line) on FTO.

$$(\alpha h\nu)^2 = C(h\nu - E_g) \tag{1}$$

$$\alpha = \frac{1}{t} \times A \times \log e \tag{2}$$

where α is the absorption coefficient of ZnO at specific wavelength values, h is Planck's constant, C is the proportionality constant, ν is the frequency of incident light, E_g is the band gap of ZnO, and t is the thickness (in cm) for the ZnO film. The estimated band gap energy for ZnO NPs is found to be ∼3.23 eV (blue line, inset to Figure 2), while the same for 1D ZnO NWs is ∼3.27 eV (red line, inset to Figure 2). Interestingly, it is observed that the absorbance spectra of

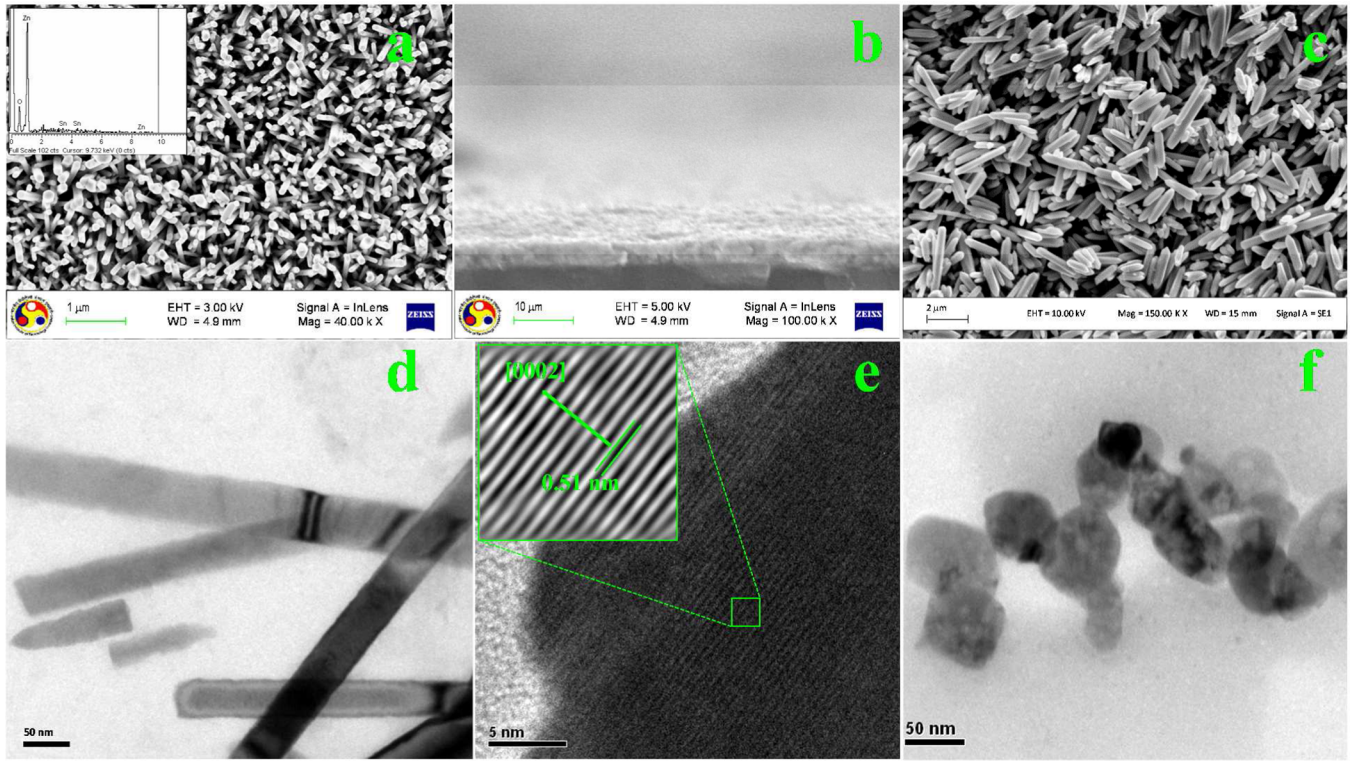

Figure 3. (a) Field-emission scanning electron microscopy (FESEM) image of 1D ZnO nanowires grown on ZnO seed layered substrates. Inset shows the energy-dispersive X-ray (EDX) spectroscopy analysis of vertically grown 1D ZnO nanowires. (b) Cross-sectional FESEM image of 1D ZnO nanowires grown on FTO substrate. (c) SEM image of hydrothermally grown bare ZnO nanowires. (d) Transmission electron microscopy (TEM) and (e) high resolution-TEM (HR-TEM) image of as-grown 1D ZnO nanowires. Inset to (e) shows the (002) lattice plane and interplanar *d*-spacing using IFFT of the HR-TEM image of 1D ZnO nanowires. (f) TEM image of as-synthesized ZnO nanoparticles.

SK1-ZnO NP (orange line) and SK1-1D ZnO NW (green line) films show the characteristic absorption profiles for both of the components, ZnO and SK1. This further confirms the enhanced molar absorptivity of ZnO (NWs and NPs) after its sensitization with the SK1 dye.

3.3. Materials Morphology. The morphologies of 1D ZnO NWs and ZnO NPs are investigated by SEM, FESEM, and TEM analysis. Figure 3a shows the representative top-down FESEM image of the as-synthesized 1D ZnO NWs grown over ZnO seed layer. The inset to Figure 1a shows the energy-dispersive X-ray (EDX) analysis of 1D ZnO NWs, confirming the presence of Zn and O atoms in the sample. The thickness of the 1D ZnO NWs grown on ZnO seeded substrates is analyzed by the cross-sectional FESEM image as shown in Figure 1b. The thickness of 1D ZnO NW layer is found to be ∼5−7 μm, which is further confirmed using the surface profilometer. To investigate the role of ZnO seed layered substrates to achieve the vertically aligned growth of 1D ZnO NWs, the SEM analysis of hydrothermally synthesized bare ZnO NWs is carried out. Figure 1c shows the SEM image of bare ZnO NWs, which clearly indicates the randomly orientated growth of ZnO NWs in the absence of ZnO seed layered substrates. The morphologies of the 1D ZnO NWs are further explored using TEM analysis, which confirms the formation of 1D shaped ZnO NWs with an average diameter of ∼45 nm. In addition, Figure 1e depicts the high-resolution TEM (HRTEM) image of 1D ZnO NWs showing the well-defined lattice fringes with an interplanar *d*-spacing of 0.51 ± 0.006 nm along the [0002] direction of ZnO crystal structure without any crystal dislocations. The inset to Figure 1e represents the inverse fast Fourier transform (IFFT) of the HRTEM image confirming an interplanar *d*-spacing of ∼0.51 nm, which is clearly assignable to the (002) lattice plane of wurtzite ZnO. The morphologies of the as-synthesized ZnO NPs are investigated by using TEM analysis. Figure 1f represents the TEM image of the ZnO NPs, which shows the formation of NPs with an average diameter of ∼50 nm.

3.4. Density Functional Theory (DFT) Study of SK1 Dye. To have an idea of the minimal energy geometric configuration and electronic density distribution of the frontier molecular orbitals of SK1 dye molecule, density functional theory (DFT) calculations are carried out using Accelrys Materials Studio 4.0. The theoretical picture of the frontier orbitals for SK1 dye was derived from the DFT approach. The molecular geometries of SK1 were optimized in DMol3 program package using generalized gradient approximation (GGA) with BLYP as the basis set. These simulations were carried out in a vacuum for the single molecule. Figure 4 shows the optimized geometry of the molecule along with electron density map for HOMO and LUMO energy levels. Figure 4 also illustrates that the electronic density distribution at the HOMO energy level of SK1 is consistently distributed over the carbazole electron donor unit and the π-conjugated oligo-phenylenevinylene unit. On the other hand, the LUMO energy level of SK1 represents the electronic excitation of the molecule resulting in the intramolecular charge transfer leading to an electron migration from the donor unit to the cyanoacrylic acceptor unit. This clearly accounts for the excited-state electron injection into the CB of ZnO via the carboxyl group attached to the carbon atom bonded with the cyano group. Moreover, the separation between the HOMO and LUMO energy levels is remarkable, allowing a long-lived excited state. A detailed representation of the frontier molecular orbitals of SK1 with energy level diagram in ZnO-based DSSCs is shown in Figure S4 (see the Supporting Information).

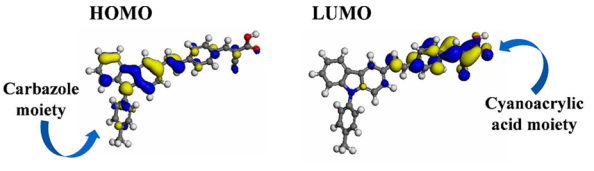

Figure 4. HOMO and LUMO frontier molecular orbitals of SK1 as calculated from the density functional theory (DFT) at a B3LYP/6-31+G(d) level showing the electronic distributions in its ground and excited states.

3.5. Steady-State Photoluminescence (PL) and Time-Resolved PL Studies. To probe the electronic interactions between SK1 and ZnO, the steady-state photoluminescence (PL) spectra of SK1 (black line), SK1-ZnO NP (blue line), and SK1-1D ZnO NW (red line) are recorded at an excitation wavelength (λ_{exc}) of 418 nm. Figure 5 shows a significant

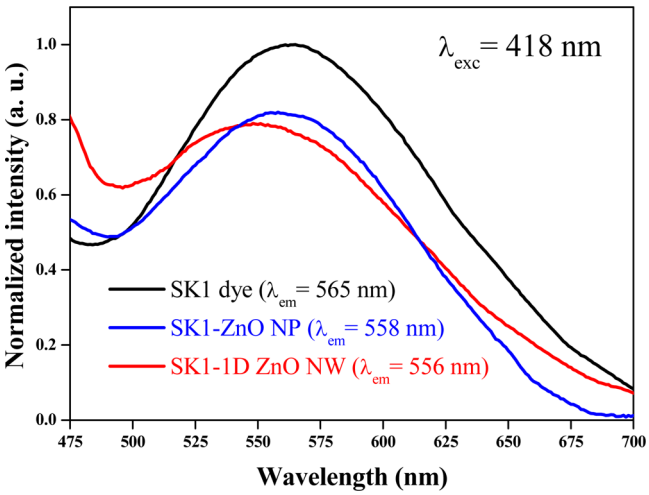

Figure 5. Steady-state photoluminescence (PL) spectra of SK1 dye film on FTO (black line), SK1-sensitized 1D ZnO nanoparticle on FTO (blue line), and SK1-sensitized 1D ZnO nanowire grown on FTO (red line) at an excitation wavelength of 418 nm.

quenching in the PL emission originating from the SK1 dye, when it is anchored onto the ZnO (NWs or NPs). This confirms the presence of excited-state electronic interactions between SK1 and ZnO, representing the deactivation of the excited dye via electron transfer to the CB of ZnO. The electrons injected from SK1 into ZnO are collected to generate the photocurrent, and the redox electrolyte scavenges the hole simultaneously. It is noteworthy that the quenching of the PL emission is more in the case of 1D ZnO NWs as compared to ZnO NPs due to the intrinsically faster charge transport property of 1D ZnO NWs over ZnO NPs.[40,41] However, a slight shift of ∼7−9 nm is observed in the PL emission maxima of SK1 after its adsorption onto ZnO NWs and NPs, which can be attributed to the strong electronic interactions between SK1 and ZnO.

To gain insight into the excited-state emission decay behavior of SK1 anchored onto ZnO, the time-resolved photoluminescence (TRPL) measurements are performed on plain SK1 (black line), SK1-ZnO NP (blue line), and SK1-1D ZnO NW (red line) films on FTO using a 405 nm diode laser

excitation, as shown in Figure 6. The detailed spectroscopic and fitting parameters (χ^2) for the emission decays for SK1, SK1-ZnO NP, and SK1-1D ZnO NW are summarized in Table 1. The excited-state emission decay lifetime (τ_1 and τ_2) values for the three films on FTO are determined from the TRPL data fitted by a biexponential function. The kinetic decay curves are fitted in the function following eq 3 using the FAST software provided by the Edinburgh instrument.

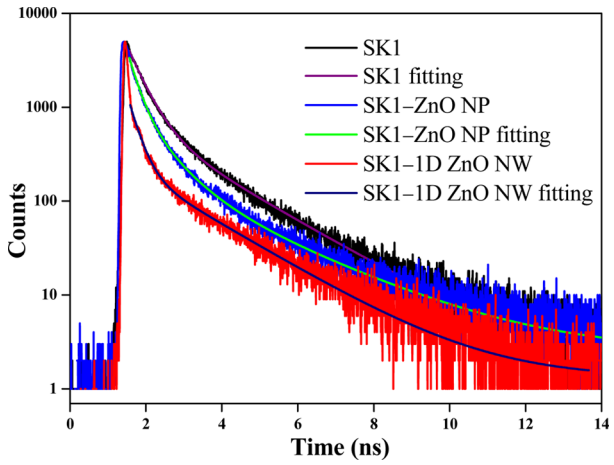

Figure 6. Time-resolved photoluminescence (TRPL) spectra of SK1 dye thin film on FTO (black line), SK1-sensitized ZnO nanoparticle film on FTO (SK1-ZnO NP, blue line), and SK1-sensitized 1D ZnO nanowires grown on FTO (SK1-1D ZnO NW, red line) with their fitting curves at an excitation wavelength of 405 nm.

$$I(t) = \sum \alpha_i \exp\left(-\frac{t}{\tau_i}\right) \quad (3)$$

where I is the normalized emission intensity, α_i is the amplitude of decay component i having a lifetime of τ, and t is the time after pulsed-laser excitation. The average excited-state lifetime ($\langle\tau\rangle$) values for the samples are derived by following eq 4:

$$\langle\tau\rangle = \sum_i \alpha_i\tau_i^2 / \sum_i \alpha_i\tau_i \quad (4)$$

The kinetic curves depicted in Figure 6 clearly indicate that in the presence of ZnO, the exciton lifetimes for SK1 are notably faster. The corresponding lifetime values for SK1 significantly decrease from ~0.41 ns (τ_1) and ~1.82 ns (τ_2) to ~0.26 and ~0.80 ns for SK1-ZnO NP and to ~0.25 and ~0.72 ns for SK1-1D ZnO NW. Similarly, the calculated average emission decay lifetime ($\langle\tau\rangle$) for SK1 is found to decrease from ~1.54 to ~0.68 ns (SK1-ZnO NP) and ~0.60 ns (SK1-1D ZnO NW). It is observed that in the SK1-sensitized photoanodes, the photoexcited charge migration from SK1 to 1D ZnO NWs is slightly higher than that in case of ZnO NPs. This could be due to the higher charge transportation in case of 1D ZnO NWs.

$$k_{ei} = 1/\tau_{(SK1\text{-}ZnO)} - 1/\tau_{(SK1)} \quad (5)$$

The aforementioned electronic interactions confirm the photoexcited electron injection from SK1 to the CB of ZnO, which is facilitated by the higher vacant energy levels of ZnO.[42] By considering this electron transfer as the only pathway for the deactivation of excited SK1, the transfer rate constants for the electron injection (k_{ei}) from SK1 to ZnO can be calculated from eq 5 and are found to be 8.29×10^8 s^{-1} (for SK1-ZnO NP) and 1.01×10^9 s^{-1} (for SK1-ZnO NW). However, it should be noted that the PL decay curves also reflect the transportation inside ZnO, recombination rate at the ZnO–dye hetero interface, and the location of the Fermi level, eventually depending on the crystal defects present in ZnO. The electron relaxation time in the ZnO architectures can be correlated with the defect-mediated emission originating from ZnO. In view of this, we have compared the PL spectra of 1D ZnO NW and ZnO NP thin films (grown/deposited on FTO substrates) at an excitation wavelength of 410 nm. The emission spectra for ZnO NWs and NPs, shown in Figure S5 (see the Supporting Information), exhibit defect-mediated emission peaks visibly in the wavelength range of ~450–580 nm. This green emission peak is attributed to the transition from the CB of ZnO to the deep defect levels of ZnO created by oxygen vacancies.[26] The defect emission peak for 1D ZnO NWs is observed to be less prominent as compared to that of the ZnO NPs, which is in good agreement with the single crystallinity of 1D ZnO NWs as obtained from the XRD patterns. The preferential unidirectional growth along the (002) direction offers less crystal defects in 1D ZnO NWs, favoring a longer excited-state relaxation time in contrast to ZnO NPs.

3.6. Electrochemical Study of SK1 Dye. The cyclic voltammetry (CV) of SK1 dye is performed in anhydrous acetonitrile in the presence of 0.1 M tetra-*n*-butylammonium hexafluorophosphate (TBAP) electrolyte to estimate its highest-occupied molecular orbital (HOMO) level. An oxidation half-potential of +1.37 V (vs NHE) has been observed for SK1 (Figure S6, Supporting Information). Using the expression $E_{HOMO} = -[E_{onset(Fc/Fc+)} + 5.1]$ eV, the HOMO energy level of SK1 is found to be at −5.62 eV (vs Fc/Fc^+), which is more positive than the redox potentials of I_3^-/I^- (−4.8 eV) and $Co^{3+/2+}$ (−5.1 eV) electrolyte. The LUMO energy level of SK1 is evaluated from its optical energy band gap (E_g) and HOMO values following the expression, $E_{HOMO} - E_{LUMO} = E_g$. From the absorption onset (Figure 2), the value of E_g for SK1 is found to be 2.25 eV. The estimated LUMO energy level for SK1 is at −3.37 eV (vs Fc/Fc^+), which is higher than the CB potential of ZnO (−4.3 eV). This affords a facilitated energy matching between the LUMO of SK1 and the CB of ZnO, resulting in a favorable electron transfer from the LUMO of the dye to the CB of ZnO.

3.7. Photovoltaic Performance. The photocurrent–voltage characteristics of the fabricated DSSCs (FTO/ZnO/SK 1 dye/Pt/FTO) are measured by employing a metal-free

Table 1. Fitting Parameter (χ^2), Initial Intensity (α_1, α_2), Excited-State Lifetime (τ_1, τ_2), and Average Exciton Lifetime ($\langle\tau\rangle$) for the SK1 Thin-Film Spin-Coated on FTO (SK1), SK1-Sensitized ZnO NPs on FTO (SK1-ZnO NP), and SK1-Sensitized 1D ZnO NWs on FTO (SK1-1D ZnO NW)

sample	χ^2	α_1	α_2	τ_1 (ns)	τ_2 (ns)	$\langle\tau\rangle$ (ns)	k_{ei} (s^{-1})
SK1	1.080	52.25	47.75	0.414	1.817	1.537	
SK1-ZnO NP	1.064	36.93	39.47	0.266	0.803	0.675	8.29×10^8
SK1-1D ZnO NW	1.041	34.69	37.31	0.250	0.716	0.602	1.01×10^9

dx.doi.org/10.1021/am5026193 | ACS Appl. Mater. Interfaces 2014, 6, 12629–12639

carbazole derivative (SK1) dye sensitizer against Pt counter electrode and the $[Co(bpy)_3]^{3+/2+}$ and I_3^-/I^- redox electrolytes under AM 1.5G simulated sunlight with a light intensity of 100 mW/cm^2, as shown in Figure 7. In the typical 1D ZnO NW-

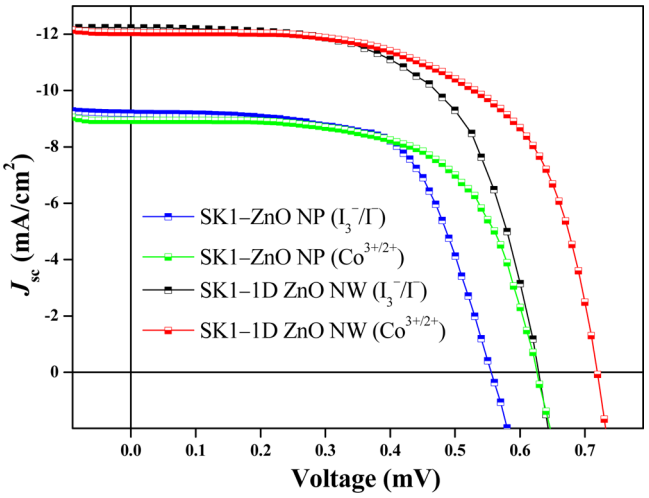

Figure 7. Comparison of the short-circuit current density−voltage (J_{sc}−V) plots for the fabricated DSSCs based on SK1-ZnO NP photoanodes employing I_3^-/I^- (blue line) and $Co^{3+/2+}$ (green line) and SK1-1D ZnO NW photoanodes employing I_3^-/I^- (black line) and $Co^{3+/2+}$ (red line) redox electrolytes.

based device, a short-circuit current density (J_{sc}) of ∼12.0 mA/cm^2, an open-circuit voltage (V_{oc}) of 719 mV, and a fill factor (FF) of 64% affording an overall PCE of ∼5.7% have been achieved by employing the $[Co(bpy)_3]^{3+/2+}$ redox electrolyte (red line). The identical device with I_3^-/I^- electrolyte (black line) exhibited a $J_{sc} \approx$ 12.2 mA/cm^2, $V_{oc} \approx$ 629 mV, and FF ≈ 61%, resulting in a PCE of ∼4.7%. In contrast, the V_{oc} has been remarkably increased by 90 mV upon the employment of the cobalt-based electrolyte over the iodide system. Similar trends are also observed in the performance of the DSSCs fabricated with ZnO NPs. The ZnO NP-based DSSC has shown a $J_{sc} \approx$ 8.79 mA/cm^2, a $V_{oc} \approx$ 626 mV, a FF ≈ 63%, and a PCE of ∼3.6% for the cobalt-based electrolyte (green line), while the respective performance in the presence of I_3^-/I^- system (blue line) is ∼9.1 mA/cm^2, ∼555 mV, ∼61%, and ∼3.2%, respectively. The enhancement in the J_{sc} and V_{oc} of the DSSCs based on 1D ZnO NWs as compared to ZnO NPs is represented in Figure S8 (see the Supporting Information). This is attributed to the rapid electron transport through the 1D pathway of ZnO NWs.

The photocurrent characteristics of the fabricated DSSCs are estimated from the incident photon-to-current conversion efficiency (IPCE) values measured at short-circuit against the wavelength. Figure 8 represents the IPCE spectra of the fabricated DSSCs exhibiting the highest values ∼60−62% (ZnO NW-based DSSC) and ∼47−48% (ZnO NP-based DSSC) for both of the redox electrolytes showing a broad plateau in the wavelength range of 300−580 nm. This ensures a saturated light absorption by the SK1 sensitizer, which is in agreement with the UV−vis absorption spectra. In addition, the proximal band edge alignments of SK1 and ZnO make it feasible to transfer the photogenerated electrons from the LUMO of SK1 to the CB of ZnO, as shown in the inset to Figure 8. Evidently, 1D ZnO NW-based DSSCs have shown a significant enhancement in the IPCE in comparison to ZnO

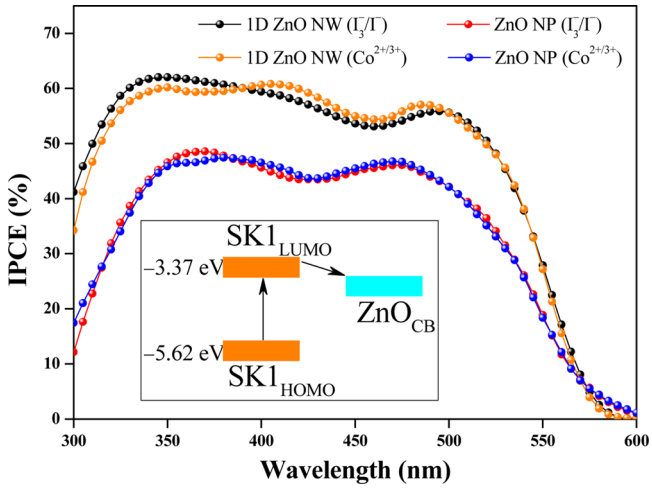

Figure 8. Comparison of incident photon-to-current conversion efficiency (IPCE) spectra using 1D ZnO nanowires and ZnO nanoparticles in the presence of $[Co(bpy)_3]^{3+/2+}$ (orange and blue lines) and I_3^-/I^- (black and red lines) redox systems. Inset shows the pathway for the photoexcited charge transfer from the lowest-unoccupied molecular orbital (LUMO) of SK1 dye to the conduction band (CB) of ZnO.

NPs due to the efficiently faster electron transport via 1D ZnO NWs over ZnO NPs. It should also be noted that for both ZnO NW- and NP-based devices, a slight enhancement in the photocurrent response in the blue region (∼390−470 nm) is endowed by $[Co(bpy)_3]^{3+/2+}$ with respect to the I_3^-/I^- electrolyte. This can be ascribed to the lower molar absorption coefficients of $[Co(bpy)_3]^{3+/2+}$ in the blue spectral region in contrast to the I_3^-/I^- electrolyte.

The overall photovoltaic performance parameters of all of the fabricated devices in the presence of both $[Co(bpy)_3]^{3+/2+}$ and I_3^-/I^- redox couples are summarized in Table 2. As can be seen (Table 2), a change in the ZnO morphology from NPs to 1D NWs in the photoanodes of the fabricated DSSCs has shown an increment in the J_{sc} values from ∼8.93−9.19 to 12.04−12.22 mA/cm^2. To have an idea about the effect of ZnO architectures (1D NW vs NP) in the J_{sc} value of the cells, the amounts of SK1 dye chemisorbed onto the ZnO surface are estimated using the dye-desorption carried out under basic conditions. First, the chemisorption of SK1 dye onto ZnO surface was confirmed by recording the FTIR spectra of the SK1, SK1-1D ZnO NW, and SK1-ZnO NP films on FTO substrates using a blank FTO as the reference (Figure S6, Supporting Information). The SK1 dye thin film shows the characteristic IR stretching bands for −COOH of SK1 molecule at ∼1787 cm^{-1} ($\nu_{C=O}$) and ∼1597 cm^{-1} (ν_{C-O}). Correspondingly, the FTIR stretching bands are also observed for SK1-1D ZnO NW (at ∼1792, ∼1599 cm^{-1}) and SK1-ZnO NP (at ∼1794, ∼1602 cm^{-1}) films on FTO substrates. The slight shifts in the IR stretching frequencies for SK1 upon anchoring on the ZnO surface confirm the chemisorption of SK1 dye over ZnO. The amounts of chemisorbed dyes on the ZnO films are found to be ∼1.37 × 10^{-7} mol cm^{-2} for SK1-1D ZnO NW and ∼1.93 × 10^{-7} mol cm^{-2} for SK1-ZnO NP. The dye-desorption experiments suggest slightly higher dye loading in the case of 1D ZnO NWs in contrast to ZnO NPs, which can also be ascribed to the lower BET surface area of ∼19.3 m^2 g^{-1} for 1D ZnO NWs as compared to ∼26.9 m^2 g^{-1} for ZnO NPs. Although the dye loading is observed to be more in ZnO NP-based photoanodes

dx.doi.org/10.1021/am5026193 | ACS Appl. Mater. Interfaces 2014, 6, 12629−12639

Table 2. Short-Circuit Current Density (J_{sc}), Open-Circuit Voltage (V_{oc}), Fill Factor (FF), Power Conversion Efficiency (η), and Maximum IPCE Values for the Fabricated Dye-Sensitized Solar Cells with Respect to Different Photoanodes and Redox Electrolytes

photoanode of the DSSCs	redox electrolyte	J_{sc} (mA/cm^2)	V_{oc} (mV)	FF (%)	η (%)	IPCE$_{max}$ (%)
SK1-1D ZnO NW	I_3^-/I^-	12.22	629	61.2	4.7	62
		(12.19 ± 0.4)	(611 ± 17)	(58.6 ± 1.2)	(4.01 ± 0.5)	
SK1-1D ZnO NW	$[Co(bpy)_3]^{3+/2+}$	12.04	719	64.6	5.7	60
		(11.99 ± 0.3)	(701 ± 26)	(63.8 ± 1.7)	(5.1 ± 0.9)	
SK1-ZnO NP	I_3^-/I^-	9.19	555	61.7	3.2	48
		(9.11 ± 0.5)	(524 ± 36)	(60.9 ± 0.9)	(3.4 ± 0.4)	
SK1-ZnO NP	$[Co(bpy)_3]^{3+/2+}$	8.93	626	63.7	3.6	47
		(8.87 ± 0.7)	(613 ± 13)	(62.9 ± 1.1)	(2.9 ± 0.2)	

as compared to 1D ZnO NWs depending on the BET surface area results, the faster electron transport pathway provided by 1D ZnO NWs predominates device performances. To confirm the longer electron lifetime facilitated by 1D ZnO NWs enhancing the electron transport in the devices, we have performed the EIS measurement of the devices under the dark conditions. EIS provides an idea regarding the comparative charge transfer and recombination processes occurring in the 1D ZnO NWs- and ZnO NPs-based DSSCs. Figure 9

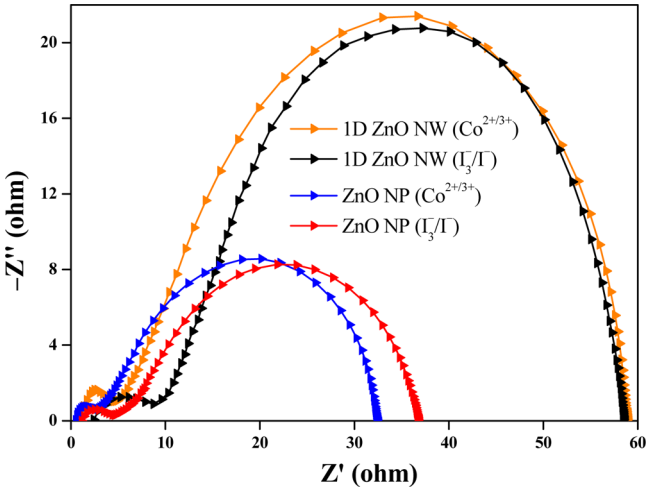

Figure 9. Nyquist plots for the fabricated DSSCs based on 1D ZnO NWs and ZnO NPs in the dark at open-circuit voltage and in a frequency range from 0.1 Hz to 100 kHz.

represents the EI spectra of the devices obtained under the darkness at the applied bias equivalent to the open-circuit voltage and a frequency range from 100 kHz to 0.1 Hz. As can be seen from Figure 9, the Nyquist plots for both NW- and NP-based cells are composed of two semicircles. The right semicircle in the medium-frequency region is due to the charge-transfer process at the ZnO/SK1 dye/electrolyte interface, and the left semicircle in the high-frequency region is ascribed to the redox reaction at the Pt/electrolyte interface. In contrast to the ZnO NP-based devices, 1D ZnO NW-based devices have shown a larger radius of the right semicircle. This corresponds to a longer electron lifetime (or increased charge-recombination resistance) in the case of 1D ZnO NWs; in other words, a longer distance is traveled by the photoexcited electrons in 1D ZnO NWs as compared to the ZnO NPs. The electron lifetime (τ_e) can be derived from the peak frequency (f_p) in the medium-frequency region using the relation $\tau_e = 1/2\pi f_p$.[43] The longer electron lifetime of 1D ZnO NWs is also resembled in the higher V_{oc} values of the 1D ZnO NW-based devices in contrast to ZnO NPs.

4. CONCLUSIONS

In summary, a metal-free carbazole dye (SK1) has been synthesized and applied as the sensitizer for 1D ZnO NW and ZnO NP-based solar cells. The combination of enhanced electron transport property of 1D ZnO NWs (over NPs) and higher molar absorption coefficient of the metal-free SK1 dye could achieve a PCE up to ∼5.7% against the Pt counter electrode in the presence of $[Co(bpy)_3]^{3+/2+}$ electrolyte. The identical device with I_3^-/I^- has shown a PCE of ∼4.7%. Similarly, the ZnO NP-based DSSCs could yield PCEs of ∼3.6% and ∼3.2% for cobalt- and iodide-based electrolytes, respectively. The enhanced rate of photogenerated electron injection and transport through the 1D ZnO NWs as compared to ZnO NPs resulted in a maximum IPCE of ∼62% for ZnO NWs, while the same for ZnO NPs is only ∼48%. The electrochemical impedance spectroscopy shows a longer electron lifetime in the 1D ZnO NW-based devices in contrast to ZnO NPs. This work further gives a scope to investigate new metal-free organic dyes for photovoltaic applications depending on the band edge alignment suitability with metal oxides.

■ ASSOCIATED CONTENT

Supporting Information

Electrochemical analysis and ^{1}H NMR spectrum for SK1 dye, frontier molecular orbitals of SK1 with energy level diagram based on DFT calculations, FTIR spectra of the dye and photoanodes, UV−vis spectra for chemisorption experiment, and comparison of J_{sc} and V_{oc} values for the DSSCs based on 1D ZnO NW and ZnO NPs. This material is available free of charge via the Internet at http://pubs.acs.org.

■ AUTHOR INFORMATION

Corresponding Authors

*Tel.: +91-2692226857 (ext 216). E-mail: soni_b21@yahoo.co.in.

*Tel.: +91-361-2582320. Fax: +91-3612582349. E-mail: mq@iitg.ernet.in.

Notes

The authors declare no competing financial interest.

■ ACKNOWLEDGMENTS

We acknowledge the Department of Science and Technology (DST), India, for financial support through project nos. DST/SR/S1/IC-25/2009, DST/TSP/2009/23, and DST/TSG/PT/2008/23 and the Council of Scientific and Industrial Research,

India, through no. 01(2704)/12/EMR-II. Infrastructure and instrumentation help from IIT Guwahati and CIF, IIT Guwahati, is acknowledged. The authors thank Ashish Singh and Rama Ghosh for their help in EIS and dye loading measurements.

REFERENCES

(1) Hagfeldt, A.; Boschloo, G.; Sun, L.; Kloo, L.; Pettersson, H. Dye-Sensitized Solar Cells. *Chem. Rev.* **2010**, *110*, 6595−6663.
(2) Balasingam, S. K.; Kang, M. G.; Jun, Y. Metal Substrate based Electrodes for Flexible Dye-Sensitized Solar Cells: Fabrication Methods, Progress and Challenges. *Chem. Commun.* **2013**, *49*, 11457−11475.
(3) Mathew, S.; Yella, A.; Gao, P.; Humphrey-Baker, R.; Curchod, B. F. E.; Ashari-Astani, N.; Tavernelli, I.; Rothlisberger, U.; Nazeeruddin, M. K.; Grätzel, M. Dye-Sensitized Solar Cells with 13% Efficiency Achieved Through the Molecular Engineering of Porphyrin Sensitizers. *Nat. Chem.* **2014**, *6*, 242−247.
(4) Yella, A.; Lee, H.-W.; Tsao1, H. N.; Yi, C.; Chandiran, A. K.; Nazeeruddin, M. K.; Diau, E. W.-G.; Yeh, C.-Y.; Zakeeruddin, S. M.; Grätzel, M. Porphyrin-Sensitized Solar Cells with Cobalt (II/III)−Based Redox Electrolyte Exceed 12% Efficiency. *Science* **2011**, *334*, 629−634.
(5) O'Regan, B.; Grätzel, M. A Low-Cost, High-Efficiency Solar Cell Based on Dye-Sensitized Colloidal TiO_2 Films. *Nature* **1991**, *353*, 737−740.
(6) Wang, Z.; Liang, M.; Wang, L.; Hao, Y.; Wang, C.; Sun, Z.; Xue, S. New Triphenylamine Organic Dyes Containing Dithieno [3,2-b:2′,3′-d]Pyrrole (DTP) Units for Iodine-Free Dye-Sensitized Solar Cells. *Chem. Commun.* **2013**, *49*, 5748−5750.
(7) Yella, A.; Humphrey-Baker, R.; Curchod, B. F. E.; Ashari-Astani, N.; Teuscher, J.; Polander, L. E.; Mathew, S.; Moser, J.-E.; Tavernelli, I.; Rothlisberger, U.; Grätzel, M.; Nazeeruddin, M. K.; Frey, J. Molecular Engineering of a Fluorene Donor for Dye-Sensitized Solar Cells. *Chem. Mater.* **2013**, *25*, 2733−2739.
(8) Mishra, A.; Fischer, M. K. R.; Buerle, P. Metal-Free Organic Dyes for Dye-Sensitized Solar Cells: From Structure: Property Relationships to Design Rules. *Angew. Chem., Int. Ed.* **2009**, *48*, 2474−2499.
(9) Ito, S.; Miura, H.; Uchida, S.; Takata, M.; Sumioka, K.; Liska, P.; Comte, P.; Péchyb, P.; Grätzel, M. High-Conversion-Efficiency Organic Dye-Sensitized Solar Cells with a Novel Indoline Dye. *Chem. Commun.* **2008**, 5194−5196.
(10) Xianga, W.; Huangb, W.; Bachbcd, U.; Spiccia, L. Stable High Efficiency Dye-Sensitized Solar Cells Based on a Cobalt Polymer Gel Electrolyte. *Chem. Commun.* **2013**, *49*, 8997−8999.
(11) Guo, K.; Yan, K.; Lu, X.; Qiu, Y.; Liu, Z.; Sun, J.; Yan, F.; Guo, W.; Yang, S. Dithiafulvenyl Unit as a New Donor for High-Efficiency Dye-Sensitized Solar Cells: Synthesis and Demonstration of a Family of Metal-Free Organic Sensitizers. *Org. Lett.* **2012**, *14*, 2214−2217.
(12) Wang, Z.- S.; Cui, Y.; Dan-oh, Y.; Kasada, C.; Shinpo, A.; Hara, K. Molecular Design of Coumarin Dyes for Stable and Efficient Organic Dye-Sensitized Solar Cells. *J. Phys. Chem. C* **2008**, *112*, 17011−17017.
(13) Li, S.-G.; Jiang, K.-J.; Huang, J.-H.; Yang, L.-M.; Song, Y.-L. Molecular Engineering of Panchromatic Isoindigo Sensitizers for Dye-Sensitized Solar Cell Applications. *Chem. Commun.* **2014**, *50*, 4309−4311.
(14) Hwang, S.; Lee, J. H.; Park, C.; Lee, H.; Kim, C.; Park, C.; Lee, M.-H.; Lee, W.; Park, J.; Kim, K.; Park, N.-G.; Kim, C. A Highly Efficient Organic Sensitizer for Dye-Sensitized Solar Cells. *Chem. Commun.* **2007**, 4887−4889.
(15) Feldt, S. M.; Gibson, E. A.; Gabrielsson, E.; Sun, L.; Boschloo, G.; Hagfeldt, A. Design of Organic Dyes and Cobalt Polypyridine Redox Mediators for High-Efficiency Dye-Sensitized Solar Cells. *J. Am. Chem. Soc.* **2010**, *132*, 16714−16724.
(16) Bai, Y.; Zhang, J.; Zhou, D.; Wang, Y.; Zhang, M.; Wang, P. Engineering Organic Sensitizers for Iodine-Free Dye-Sensitized Solar Cells: Red-Shifted Current Response Concomitant with Attenuated Charge Recombination. *J. Am. Chem. Soc.* **2011**, *133*, 11442−11445.
(17) Tsao, H. N.; Yi, C.; Moehl, T.; Yum, J.-H.; Zakeeruddin, S. M.; Nazeeruddin, M. K.; Grätzel, M. Cyclopentadithiophene Bridged Donor-Acceptor Dyes Achieve High Power Conversion Efficiencies in Dye-Sensitized Solar Cells Based on the Tris-Cobalt Bipyridine Redox Couple. *ChemSusChem* **2011**, *4*, 591−594.
(18) Zhou, D.; Yu, Q.; Cai, N.; Bai, Y.; Wang, Y.; Wang, P. Efficient Organic Dye-Sensitized Thin-Film Solar Cells Based on the Tris(1,10-phenanthroline)cobalt(II/III) Redox Shuttle. *Energy Environ. Sci.* **2011**, *4*, 2030−2034.
(19) Kashif, M. K.; Nippe, M.; Duffy, N. W.; Forsyth, C. M.; Chang, C. J.; Long, J. R.; Spiccia, L.; Bach, U. Stable Dye-Sensitized Solar Cell Electrolytes Based on Cobalt(II)/(III) Complexes of a Hexadentate Pyridyl Ligand. *Angew. Chem., Int. Ed.* **2013**, *52*, 5527−5531.
(20) Teng, C.; Yang, X.; Yuan, C.; Li, C.; Chen, R.; Tian, H.; Li, S.; Hagfeldt, A.; Sun, L. Two Novel Carbazole Dyes for Dye-Sensitized Solar Cells with Open-Circuit Voltages up to 1 V Based on Br^-/Br_3^- Electrolytes. *Org. Lett.* **2009**, *11*, 5542−5545.
(21) De Sousa, S.; Olivier, C.; Ducasse, L.; Le Bourdon, G.; Hirsch, L.; Toupance, T. *ChemSusChem* **2013**, *6*, 993−996.
(22) Teng, C.; Yang, X.; Li, S.; Cheng, M.; Hagfeldt, A.; Wu, L.; Sun, L. Tuning the HOMO Energy Levels of Organic Dyes for Dye-Sensitized Solar Cells Based on Br^-/Br_3^- Electrolytes. *Chem.—Eur. J.* **2010**, *16*, 13127−13138.
(23) Anta, J. A.; Guillén, E.; Tena-Zaera, R. ZnO-Based Dye-Sensitized Solar Cells. *J. Phys. Chem. C* **2012**, *116*, 11413−11425.
(24) Li, L.; Zhai, T.; Bando, Y.; Golberg, D. Recent Progress of One-Dimensional ZnO Nanostructured Solar Cells. *Nano Energy* **2012**, *1*, 91−106.
(25) Zhang, Q.; Cao, G. Nanostructured Photoelectrodes for Dye-Sensitized Solar Cells. *Nano Today* **2011**, *6*, 91−109.
(26) Chetia, T. R.; Barpuzary, D.; Qureshi, M. Enhanced Photovoltaic Performance Utilizing Effective Charge Transfers and Light Scattering Effects by the Combination of Mesoporous, Hollow 3D-ZnO along with 1D-ZnO in CdS Quantum Dot Sensitized Solar Cells. *Phys. Chem. Chem. Phys.* **2014**, *16*, 9625−9633.
(27) Ren, S.; Zhao, N.; Crawford, S. C.; Tambe, M.; Bulović, V.; Gradečak, S. Heterojunction Photovoltaics Using GaAs Nanowires and Conjugated Polymers. *Nano Lett.* **2010**, *11*, 408−413.
(28) Ren, S.; Chang, L.-Y.; Lim, S.-K.; Zhao, J.; Smith, M.; Zhao, N.; Bulović, V.; Bawendi, M. G.; Gradečak, S. Inorganic−Organic Hybrid Solar Cell: Bridging Quantum Dots to Conjugated Polymer Nanowires. *Nano Lett.* **2011**, *11*, 3998−4002.
(29) Sun, B.; Hao, Y.; Guo, F.; Cao, Y.; Zhang, Y.; Li, Y.; Xu, D. Fabrication of Poly(3-hexylthiophene)/CdS/ZnO Core−Shell Nanotube Array for Semiconductor-Sensitized Solar Cell. *J. Phys. Chem. C* **2012**, *116*, 1395−1400.
(30) Zhang, Q.; Dandeneau, C. S.; Zhou, X.; Cao, G. ZnO Nanostructures for Dye-Sensitized Solar Cells. *Adv. Mater.* **2008**, *21*, 4087−4108.
(31) Barpuzary, D.; Qureshi, M. Enhanced Photovoltaic Performance of Semiconductor-Sensitized ZnO−CdS Coupled with Graphene Oxide as a Novel Photoactive Material. *ACS Appl. Mater. Interfaces* **2013**, *5*, 11673−11682.
(32) Park, H.; Chang, S.; Jean, J.; Cheng, J. J.; Araujo, P. T.; Wang, M.; Bawendi, M. G.; Dresselhaus, M. S.; Bulović, V.; Kong, J.; Gradečak, S. Graphene Cathode-Based ZnO Nanowire Hybrid Solar Cells. *Nano Lett.* **2013**, *13*, 233−239.
(33) Liu, B.; Zeng, C. Hydrothermal Synthesis of ZnO Nanorods in the Diameter Regime of 50 nm. *J. Am. Chem. Soc.* **2003**, *125*, 4430−4431.
(34) Barpuzary, D.; Khan, Z.; Vinothkumar, N.; De, M.; Qureshi, M. Hierarchically Grown Urchinlike CdS@ZnO and $CdS@Al_2O_3$ Heteroarrays for Efficient Visible-Light-Driven Photocatalytic Hydrogen Generation. *J. Phys. Chem. C* **2012**, *116*, 150−156.
(35) Liu, Y.; Jennings, J. R.; Huang, Y.; Wang, Q.; Zakeeruddin, S. M.; Grätzel, M. Cobalt Redox Mediators for Ruthenium-Based Dye-Sensitized Solar Cells: A Combined Impedance Spectroscopy and

Near-IR Transmittance Study. *J. Phys. Chem. C* **2011**, *115*, 18847−18855.
(36) Chou, T. P.; Zhang, Q.; Cao, C. Effects of Dye Loading Conditions on the Energy Conversion Efficiency of ZnO and TiO_2 Dye-Sensitized Solar Cells. *J. Phys. Chem. C* **2007**, *111*, 18804−18811.
(37) Fan, K.; Liu, M.; Peng, T.; Maa, L.; Dai, K. Effects of Paste Components on the Properties of Screen-Printed Porous TiO_2 Film for Dye-Sensitized Solar Cells. *Renewable Energy* **2010**, *35*, 555−561.
(38) Vayssieres, L. Growth of Arrayed Nanorods and Nanowires of ZnO from Aqueous Solutions. *Adv. Mater.* **2003**, *15*, 464−466.
(39) Chung, J.; Myoung, J.; Oh, J.; Lim, S. Synthesis of a ZnS Shell on the ZnO Nanowire and Its Effect on the Nanowire-Based Dye-Sensitized Solar Cells. *J. Phys. Chem. C* **2010**, *114*, 21360−21365.
(40) Zhan, X.; Wang, Q.; Wang, F.; Wang, Y.; Wang, Z.; Cao, J.; Safdar, M.; He, J. Composition-Tuned ZnO/$Zn_xCd_{1-x}Te$ Core/Shell Nanowires Array with Broad Spectral Absorption from UV to NIR for Hydrogen Generation. *ACS Appl. Mater. Interfaces* **2014**, *6*, 2878−2883.
(41) Jeong, S.; Choe, M.; Kang, J.-W.; Kim, M. W.; Jung, W. G.; Leem, Y.-C.; Chun, J.; Kim, B.-J.; Park, S.-J. High-Performance Photoconductivity and Electrical Transport of ZnO/ZnS Core/Shell Nanowires for Multifunctional Nanodevice Applications. *ACS Appl. Mater. Interfaces* **2012**, *4*, 17−23.
(42) Kongkanand, A.; Tvrdy, K.; Takechi, K.; Kuno, M.; Kamat, P. V. Quantum Dot Solar Cells. Tuning Photoresponse through Size and Shape Control of CdSe−TiO_2 Architecture. *J. Am. Chem. Soc.* **2008**, *130*, 4007−4015.
(43) Peng, W.; Han, L.; Wang, Z. Hierarchically Structured ZnO Nanorods as an Efficient Photoanode for Dye-Sensitized Solar Cells. *Chem.—Eur. J.* **2014**, *20*, 8483−8487.